# Ultraviolet $\pi$-plasmon contribution to the transverse optical response of doped single-walled carbon nanotubes

M. V. Shuba [*] and G. Valušis [†]
*Optoelectronics Department, Center for Physical Sciences and Technology, Sauletekio av. 3, Vilnius LT-10257, Lithuania*

V. A. Saroka
*Department of Physics, University of Rome Tor Vergata and INFN, Via della Ricerca Scientifica 1, 00133 Roma, Italy*

(Received 1 December 2023; revised 7 February 2024; accepted 21 March 2024; published 4 April 2024)

A model for the effective permittivity of a doped single-walled carbon nanotube (CNT) thin film in the optical range is proposed. The permittivity of CNT walls is calculated from the quantum theory of $\pi$-electron transitions. The contributions from $\sigma$ electrons and ultraviolet $\pi$ plasmon are taken into account phenomenologically using experimental data obtained for graphene and CNT film. These contributions lead to an enhancement of the depolarization effect thereby strongly suppressing the transverse response of the CNTs. They also cause a decrease in both the frequency and height of the absorption peak associated with the azimuthal intersubband plasmon in doped CNTs. This eliminates the existing discrepancy between experimental and previous theoretical data. The azimuthal plasmon response is studied in a bundle of doped CNTs.

DOI: 10.1103/PhysRevB.109.165409

## I. INTRODUCTION

There are many experimental studies wherein optical parameters of single-walled carbon nanotube (CNT) thin films have been measured [1–9]. In these studies the theoretical description usually comes down to fitting the absorption or permittivity spectrum of a CNT film with a Drude-Lorentz formula [1]. Concurrently, the quantum model of $\pi$-electron transitions [10–12] is considered to be the most appropriate to determine the frequency and strength of the optical transitions in CNTs [1,6–9]. Although, the attempt has been made in Ref. [10] to adopt this model for the description of the permittivity of a CNT film, the developed approach has not been used by the experimental groups [1–9]. One of the reasons is that the model cannot quantitatively describe a $\pi$ plasmon in CNTs [13,14].

$\pi$ plasmon occurs in the ultraviolet range 4–6 eV and significantly contributes to the CNT absorption in the wide spectral range 0.5–6.5 eV [1,15]. It is associated with a mixture of interband transitions from the electronic $\pi$ bound states to the $\pi^*$ excited states at the saddle point (M) in the band structures [10,13,14]. Those transitions lead to a surface plasmon excitation in CNTs [13,16] and graphene [16–18] and to longitudinal electron oscillations in graphite [16,19]. The frequency and form of the $\pi$-plasmon absorption band are determined by excitonic effects [20] and the interference effect between the discrete and continuum spectra of the optical transitions [21]. It has been shown that the height of $\pi$-plasmon absorption peak varies with temperature [22] and number of defects [7]. Its central frequency depends on the tube diameter [9,14] and is red shifted due to strong *e-h* interactions of the quasiparticles near the 2D saddle-point singularity [18]. Note also that various models predict different values for the $\pi$-plasmon frequency (see Fig. 1 in [23]).

The contribution from the $\pi$ plasmon to the absorption spectrum is considered additive [1]. However, this is valid only for the axial response of the CNT. The transverse response of CNT is significantly affected by the depolarization field [10,24,25], which depends on the surface conductivity of the CNT along the circumferential direction. The contribution of $\pi$ plasmon to the transverse response of CNTs has been taken into account in Ref. [26], where the nanotube is modeled as a prolate spheroid with the effective permittivity described by the Drude-Lorentz formula. However, the $\pi$-plasmon contribution has been omitted when studying the azimuthal plasmon in CNTs in the frame of both the rigorous model of $\pi$-electron transitions [27–29] and simplified model of the Drude conductivity [30,31]. The transitions from occupied $\sigma$ bands have been also ignored in those models. For such approximations, the calculated height of the azimuthal plasmon absorption peak turns out to be greater than observed in the experiment (compare experimental data in Fig. 5 in [1] with theoretical data in Fig. 6 in [27]), and the plasmon frequency is found to be blue shifted by 0.1 eV as compared to measured value (see Fig. 6(b) in [1]). These discrepancies have been proposed to be explained (i) by additional losses in the conductive environment [32] or (ii) by modification of the exciton binding energy due to the bundling of CNTs [28,33].

In this paper, we propose to calculate the conductivity of CNTs using a quantum model of $\pi$-electron transitions [10] and phenomenologically taking into account the contributions from both $\pi$ plasmon and $\sigma$ electrons. Choosing the parameters of $\pi$ plasmon, we assume that the real part of the permittivity of CNT walls should be similar to that of

[*] mikhail.shuba@ftmc.lt
[†] gintaras.valusis@ftmc.lt

 

graphene. This approach makes it possible to quantitatively describe the optical parameters of CNT films from the microscopic consideration and eliminate the discrepancy between theory and experiment when describing the response from azimuthal plasmon in doped CNTs. We explain why the azimuthal plasmon is observed during electrostatic doping of CNTs in the ionic liquid [1,26,34–38] and only for heavily doped CNT films in the air [39–41]. Finally, we also investigate the transverse optical response of a doped CNT bundle.

## II. EFFECTIVE-PERMITTIVITY MODEL

Let us consider a thin film composed of randomly dispersed single-walled CNTs embedded in the host medium with the permittivity $\kappa$. The film thickness is much less than the length of CNTs, so we assume that all the tubes are randomly oriented within the film plane. The chosen CNTs are described by the dual index $(a, b)$ and chiral angle $\theta_{ab} = \arctan[\sqrt{3}b/(2a+b)]$. We designate the single index $j$ to identify the type of CNTs with uniquely specified structures. Following Ref. [10], we use a tubule index $(a, b)$ satisfying $a \geqslant 1$ and $-a+1 \leqslant b \leqslant 0$, so that $-\pi/3 \leqslant \theta_{ab} \leqslant 0$. In this case, the index $j$ enumerates the types of CNTs with different dual indexes $(a, b)$.

Typically, the CNT is modeled as a hollow cylinder with infinitely thin wall having the surface conductivity $\sigma_{||}^{(j)}$ and $\sigma_{\perp}^{(j)}$ along the axial and circumferential directions, respectively. To compute $\sigma_{||,\perp}^{(j)}$, we use a quantum theory of $\pi$-electron transitions, where the energy band structure of CNT is calculated in the tight-binding approximation (see Appendix A and Ref. [10]). The contribution of the transitions from occupied $\sigma$ bands, $\varepsilon_\sigma = 1.4$, is included phenomenologically in $\sigma_{||,\perp}^{(j)}$ [see Eqs. (A3), (A4), (A9), and (A10) in Appendix A].

Nowadays, there is no direct measurements of the surface conductivity of individual CNTs in the optical range, while the surface conductivity of graphene is well established in experiment [17]. Very often, the measured optical data for the graphene are represented via the effective permittivity assuming the thickness of graphene layer to be 0.34 nm. For comparison of the optical parameters of CNTs with those of graphene, we assume in our further analysis that the tube walls have a finite thickness of $d = 0.34$ nm. The permittivity of the CNT wall along the axial and circumferential directions at angular frequency $\omega$ can be found as

$$\varepsilon_{||,\perp}^{(j)} = 1 + \frac{4\pi i \sigma_{||,\perp}^{(j)}}{\omega d}. \tag{1}$$

Let us introduce the CNT wall permittivity averaged over all types of CNTs in the film as

$$\overline{\varepsilon}_{||,\perp} = f^{-1} \sum_j f_j \varepsilon_{||,\perp}^{(j)}. \tag{2}$$

Here $f_j$ is a volume fraction of CNTs of type $j$ conceived as hollow cylinders of volume $2\pi R_j L d$, where $L$ and $R_j$ are the length and radius of CNT, respectively. $f$ denotes the volume fraction occupied by all CNTs, $f = \sum_j f_j$. Since no finite-length effect [42] is expected above 0.4 eV, for simplicity, the distribution function $N_j(L)$ describing the number density of CNTs of type $j$ and length $L$ will be taken the same for all types of CNTs. Then $f_j$ depends on $R_j$ and does not depend on $L$.

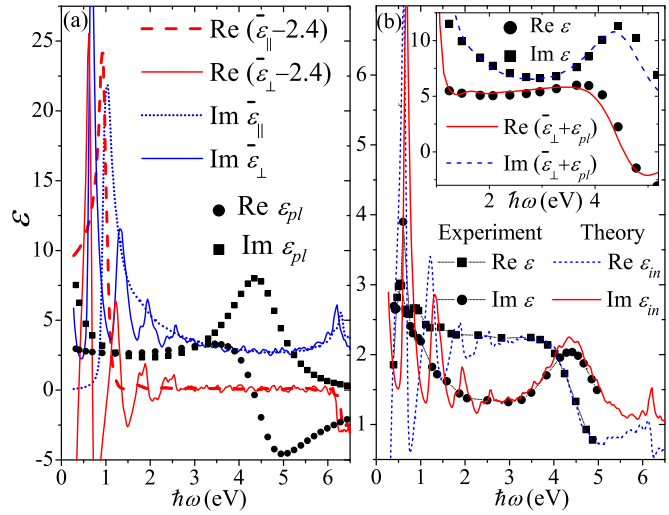


FIG. 1. (a) Frequency dependencies of the real and imaginary parts of $\overline{\varepsilon}_{||,\perp} - 2.4$ and $\varepsilon_{pl}$. (b) Frequency dependencies of the real and imaginary parts of the CNT film permittivity. Symbols: experimental data taken from Fig. 1(c) of Ref. [3]. Solid and dashed lines: theoretical results. The inset show the comparison of experimental data (symbols) for the permittivity of graphene on $SiO_2$/Si substrate from Table A1 of Ref. [17] and calculated data (lines) for the average permittivity of CNT wall $\overline{\varepsilon}_{\perp} + \varepsilon_{pl}$ along circumferential direction.

All our numerical calculations will be done for the film comprising 56 all possible types of CNTs with radii between 1.35 and 1.55 nm at electron relaxation time $\tau = 13.2$ fs. Carbon nanotubes of similar radii are often used in experimental studies [1,34–36]. Chosen relaxation time has also been used in [27,28]; it corresponds to the bandwidth of the electronic transitions detected in individual CNTs by Rayleigh scattering [43]. The number densities of CNTs of different types are taken to be the same, so that $f_j/f = R_j/\sum_j R_j$.

Let us now consider the contribution to the permittivity from $\pi$-electron transitions, $\overline{\varepsilon}_{||,\perp} - 2.4$ [here $2.4 = 1 + \varepsilon_\sigma$, see (A4) in Appendix A]. The frequency dependencies of $\mathrm{Re}(\overline{\varepsilon}_{||,\perp} - 2.4)$ and $\mathrm{Im}\ \overline{\varepsilon}_{||,\perp}$ for chosen CNT film are represented in Fig. 1(a). If one ignores the oscillations due to interband transitions below 3 eV, one may conclude that the spectra of $\overline{\varepsilon}_{||}$ and $\overline{\varepsilon}_{\perp}$ coincide well with each other in the spectral range 1–6 eV. Both spectra have resonance behavior at 6.2 eV due to a mixture of interband transitions at the saddle point in the band structure. The total contribution of all the transitions into the real part of the average CNT permittivity vanishes in the spectral range 2.5–6 eV.

For comparison, the permittivity spectrum of CNT thin film measured in [3] is represented by symbols in Fig. 1(b). One can see a resonance behavior at 4.5 eV associated with $\pi$-plasmon excitation.

The $\pi$-plasmon contribution to the permittivity of graphene sheet is well known from experiment [17] [see symbols in the inset of Fig. 1(b)]: the real part of graphene permittivity varies between 5 and 6 in the broad spectral range 1–4 eV, and its imaginary part corresponds to an asymmetrical Fano-line shape of $\pi$-plasmon absorption peak [18]. We shall suppose

that the $\pi$ plasmon contributes in a similar way to both graphene and CNT wall permittivities.

For the theoretical description of the experimental data, we propose to add in (1) an extra term

$$\varepsilon_{pl} = \varepsilon'_{pl} + i\varepsilon''_{pl}, \tag{3}$$

determining phenomenologically the contribution from $\pi$ plasmon.

We choose $\varepsilon''_{pl}$ in a way to take into account the Fano line shape [21] of $\pi$-plasmon absorption peak

$$\varepsilon''_{pl}(\omega) = \frac{\omega_0}{\omega}\frac{(qv_r/2+\omega-\omega_r)^2}{(\omega-\omega_r)^2+(v_r/2)^2}, \tag{4}$$

whereas $\varepsilon'_{pl}$ is determined by the Kramers-Kronig relation

$$\varepsilon'_{pl}(\omega) = \frac{2}{\pi}\int_0^\infty \frac{\omega'\varepsilon''_{pl}(\omega')}{\omega'^2-\omega^2}d\omega'. \tag{5}$$

Here $\omega_r$ and $v_r$ are the frequency and bandwidth of the $\pi$-plasmon peak, which can be found from the measured absorption spectrum of CNT film. The frequency $\omega_0$ in (4) should be chosen such that $\mathrm{Re}(\overline{\varepsilon}_{||,\perp}+\varepsilon_{\mathrm{pl}}) \approx 5$ in the spectral range 2–3 eV that corresponds to the real part of the measured graphene permittivity [17] [see inset in Fig. 1(b)]. The restriction on a choice of $\omega_0$ comes from expected similarity of the mechanism of $\pi$-plasmon excitation in graphene and CNTs. The factor $q$ in (4) is responsible for the Fano line shape; it can be determined by fitting the measured CNT film permittivity with the calculated one.

The phenomenological term $\varepsilon_{pl}$ is associated with the extra contribution to the CNT surface conductivity

$$\sigma_{pl} = -i\omega d\varepsilon_{pl}/4\pi, \tag{6}$$

which is assumed to be the same along the axial and circumferential directions.

Using the effective medium theory and neglecting the local field effect, the in-plane and out-of-plane effective permittivities of CNT film can be found as

$$\varepsilon_{\mathrm{in,out}} = 1+(\kappa-1)(1-f)+\frac{4\pi i f\sigma_{\mathrm{in,out}}}{\omega d}, \tag{7}$$

where the second and third terms describe the contributions from the host medium and CNTs, respectively. $\sigma_{\mathrm{in,out}}$ are the effective CNT surface conductivities in-plane and out-of-plane of CNT film,

$$\sigma_{\mathrm{in}} = 0.5(\overline{\sigma}_{||}+\overline{\sigma}_{pl||}+0.5\overline{\sigma}_{\perp}), \quad \sigma_{\mathrm{out}} = 0.5\overline{\sigma}_{\perp}, \tag{8}$$

where $\overline{\sigma}_{||}$ and $\overline{\sigma}_{pl||}$ are the average axial surface conductivities due to $\sigma$- and $\pi$-electron transitions and $\pi$-plasmon excitation, respectively,

$$\overline{\sigma}_{||} = f^{-1}\sum_j \sigma_{||}^{(j)} f_j, \quad \overline{\sigma}_{pl||} = \sigma_{pl}, \tag{9}$$

and $\overline{\sigma}_{\perp}$ is the average effective surface conductivity along the circumferential direction,

$$\overline{\sigma}_{\perp} = f^{-1}\sum_j f_j \frac{\sigma_{\perp}^{(j)}+\sigma_{pl}}{1+i2\pi(\sigma_{\perp}^{(j)}+\sigma_{pl})/\omega R_j\kappa}. \tag{10}$$

The factor 0.5 before brackets in (8) takes into account random orientations of CNTs in the plane of the film, whereas the factor 0.5 before $\overline{\sigma}_{\perp}$ is due to the cylindrical form of CNT surface. The denominator in (10) accounts for the depolarization field, which occurs when the incident electric field is polarized perpendicular to the CNT axis [10,25]. Note that $\sigma_{\perp}^{(j)}$ in the denominator of (10) includes phenomenologically the contribution from $\sigma$ electrons [see (A9) and (A10) in Appendix A]. Via the depolarization field, this contribution influences the frequency and height of azimuthal plasmon peak in doped CNTs (see Sec. III), and it has not been taken into account in previous theoretical papers [27,28].

The best fit of (7) to the permittivity spectrum observed for densified CNT film in Ref. [3] [see Fig. 1(b)] yields $q=-10$, $\hbar\omega_r = 4.5\,\mathrm{eV}$, $\hbar v_r = 1.4\,\mathrm{eV}$, and $\hbar\omega_0 = 0.35\,\mathrm{eV}$ at $\kappa = 1$ and $f = 0.39$. The value $f = 0.39$ corresponds to the carbon density 0.86 g/cm$^3$, that is close to 0.89 g/cm$^3$ declared for densified CNT film [44]. Interestingly, the average permittivity of CNT wall along the circumferential direction $\overline{\varepsilon}_{\perp}+\varepsilon_{pl}$ at chosen parameters $q$, $\omega_0$, $\omega_r$, and $v_r$ practically coincides with the graphene permittivity in the spectral range 1.2–5 eV [compare the experimental and calculated data in the inset of Fig. 1(b)]. This indicates that the obtained $\pi$-plasmon bandwidth $v_r$ for considered CNT film is determined to a greater extent by the plasmon lifetime in each CNTs and to a lesser extent by the inhomogeneous broadening caused by the dependence of plasmon frequency on the nanotube diameter [9,14].

Let us notice that we can trust the theoretical data in Fig. 1(b) only below 5.5 eV. The resonance behavior at 6.2 eV due to the transitions at the saddle point should be related to the $\pi$ plasmon. Since we take into account $\pi$ plasmon in a phenomenological way, those transitions should be excluded from consideration.

The CNT absorption cross section averaged over all types of the tubes and over all their orientations in the film is proportional to Re $\sigma_{\mathrm{in}}$ and Re $\sigma_{\mathrm{out}}$ for in-plane and out-of-plane polarizations of the incident field, respectively. Figure 2(a) represents the frequency dependencies of the real parts of $\sigma_{\mathrm{out}}$, $\sigma_{\mathrm{in}}$ and their components $0.5\overline{\sigma}_{||}$, $0.5\overline{\sigma}_{pl||}$, and $0.25\overline{\sigma}_{\perp}$ introduced in (8). As shown in Fig. 2(a), the spectrum of $0.5\mathrm{Re}\,\overline{\sigma}_{||}$ has a peaky structure due to interband electron transitions, whereas the spectrum of $0.25\overline{\sigma}_{\perp}$ is smoothed and strongly reduced due to strong depolarization effect in the transverse direction. Thus, in spite of the similar average CNT wall permittivities along the axial and circumferential directions [see Fig. 1(a)], the optical absorption in undoped CNT film occurs mostly by the axial current excitation in CNTs, so that inequality Re $\sigma_{\mathrm{in}} \gg$ Re $\sigma_{\mathrm{out}}$ remains true below 4.5 eV [see Fig. 2(a)].

As reported in [10,24,25], the depolarization effect reduces the effective surface conductivity along circumferential direction of CNT. Here we notice even stronger reduction caused by $\pi$ plasmon [see the contribution of $\sigma_{pl}$ to the denominator in (10)]. Note that the impact of the depolarization effect decreases as the host permittivity $\kappa$ increases [see Eq. (10)].

To illustrate the influence of the depolarization effect, we represent in Fig. 2(b) the frequency dependence of $0.25\,\mathrm{Re}\,\overline{\sigma}_{\perp}$ with ($\varepsilon_{pl} \neq 0$) and without ($\varepsilon_{pl} = 0$) $\pi$-plasmon contribution in the air ($\kappa = 1$) and in the dielectric host medium ($\kappa = 2$).

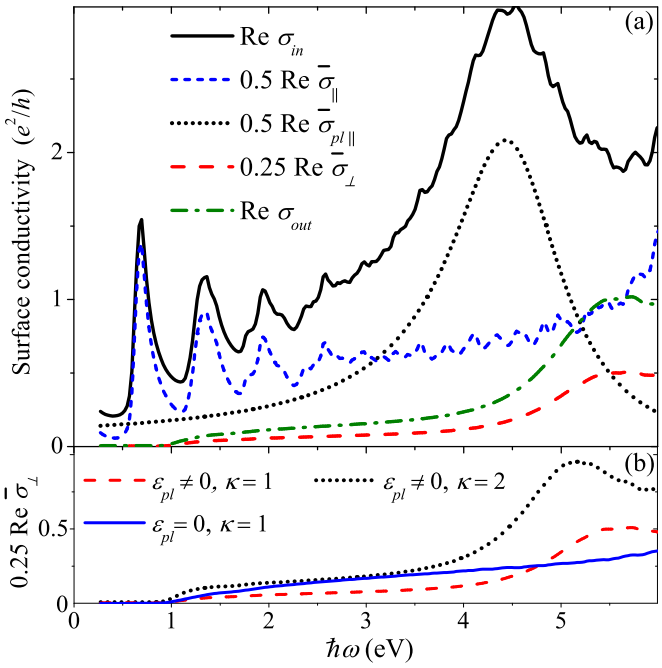


FIG. 2. (a) Frequency dependencies of Re $\sigma_{\text{in,out}}$ and its components presented in (8) at $\kappa = 1$. (b) Frequency dependencies of $0.25\,\text{Re}\,\bar{\sigma}_{\perp}$ (in units $e^2/h$) with ($\varepsilon_{pl} \neq 0$) and without ($\varepsilon_{pl} = 0$) $\pi$-plasmon contribution for CNTs in the air ($\kappa = 1$) and in the dielectric host medium ($\kappa = 2$). $e$ is an electron charge; $h$ is the Planck constant.

One can see that the real part of the effective surface conductivity along circumferential direction below 4.5 eV is smaller when the contribution from $\pi$ plasmon is taken into account [compare lines at $\kappa = 1$ in Fig. 2(b)]. This conductivity is almost twofold increases as the host permittivity $\kappa$ increases from 1 to 2 [compare lines at $\varepsilon_{pl} \neq 0$ in Fig. 2(b)].

Thus, we propose a model for the effective permittivity of CNT film. Its effectiveness for the description of the absorption spectra of doped CNT films is shown in the next section.

### III. INTERSUBBAND PLASMON IN DOPED CNTs

If the Fermi level shifts to the valence or conduction band, the intersubband transitions within the band occur for the incident field directed perpendicular to the tube axis [see (A12) in Appendix A]. As a result, an azimuthal surface plasmon can be excited in CNT in the spectral range just above the transition frequencies [27,28,31]. It is also referred to as intersubband plasmon [27,28]. Charge distribution, current oscillations, and nonzero field components $E_{\rho,\theta}$ and $H_z$ for the azimuthal plasmon are schematically represented in Fig. 3(a). For comparison, Fig. 3(b) shows axial azimuthally symmetrical surface plasmon in CNT excited by axial component of the incident field. Such plasmon occurs in the far-infrared range [45,46] and on the high-frequency side of the interband electron transitions [47].

The calculated optical densities (OD) of 80-nm thick CNT film at various Fermi energies $E_F$ are shown in Figs. 4(a) and 4(b) for the host permittivities $\kappa = 1$ and $\kappa = 2$, respectively. The parameters of CNTs in the film are taken

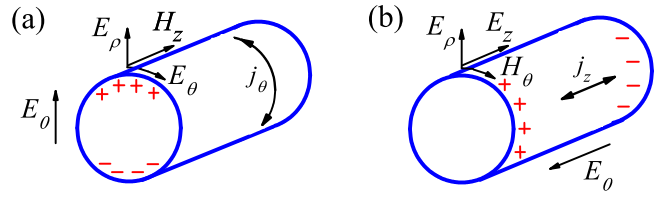


FIG. 3. Schematic illustration of the charge distribution, current oscillations $j_{\theta,z}$, and nonzero field components $E_{\theta,\rho,z}$ and $H_{\theta,z}$ for the azimuthal (a) and axial (b) TM modes excited in CNT by the incident field $E_0$.

the same as in Sec. II. Figures 4(a) and 4(b) show that the OD spectrum for undoped film ($E_F = 0$) has three peaks at 0.68, 1.34, and 1.95 eV due to interband transitions $S11$ and $S22$ in semiconducting tubes and transition $M11$ in metallic CNTs, respectively [16]. With increasing doping level, the low-energy transitions become forbidden due to the Pauli exclusion principle [27,28]. At $E_F = 0.8$ eV, the transitions $S11$ and $S22$ disappear, and a peak at 1.1 eV caused by the intersubband plasmon arises. Transformation of this peak with Fermi energy variation in Fig. 4(b) is very similar to that observed in experiments [1,34–36]. For CNTs embedded into the host medium with smaller permittivity, the depolarization effect is stronger and the peak height is smaller [compare Figs. 4(a) and 4(b) at $\kappa = 1$ and $\kappa = 2$, respectively]. This explains why the intersubband plasmon has not been detected in doped CNT film in the air [48], but it has been visible in the liquid environment [1,26,34–38]. Only recently, the

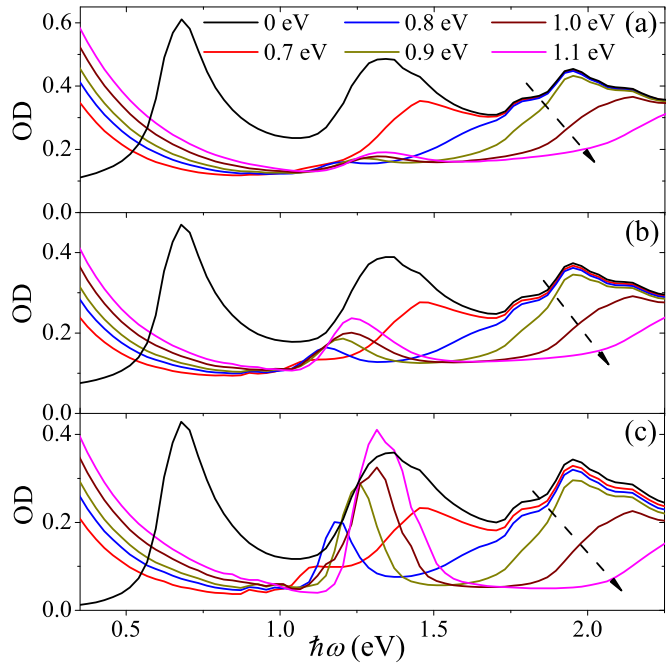


FIG. 4. Calculated frequency dependencies of the optical density (OD) of CNT film with thickness of 80 nm at various doping levels $E_F \in \{0, 0.7, 0.8, 0.9, 1.0, 1.1\}$ eV at $\kappa = 1$ (a), $\kappa = 2$ (b) and (c). The arrow indicates a direction of Fermi energy increasing. The $\pi$-plasmon and $\sigma$-electron transitions are not taken into account in (c), $\sigma_{pl} = 0$, $\varepsilon_\sigma = 0$.

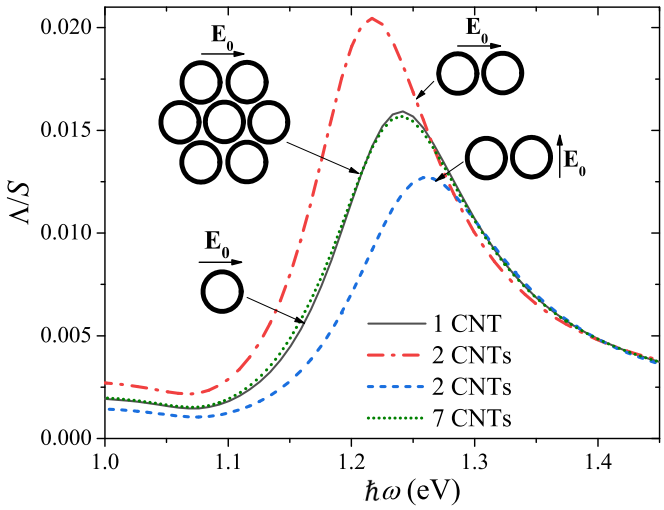


FIG. 5. Frequency dependencies of the normalized absorption cross section of a doped individual CNT, pair of CNTs, and bundle of seven CNTs. All the CNTs are identical with tubule index (0,17) at doping level $E_F = 1.1$ eV and intertube distance 0.34 nm. The orientations of the incident field $\mathbf{E}_0$ are indicated with arrows.

intersubband plasmon peak has been observed in highly doped CNT films in the air [39–41].

Figure 4(c) represents the results of the same calculations as in Fig. 4(b) but assuming $\sigma_{pl} = 0$ in (9) and (10) and $\varepsilon_\sigma = 0$ in (A10) that corresponds to the exclusion of $\pi$-plasmon and $\sigma$-electron transitions from consideration. In this case, we obtain higher frequency and height of intersubband plasmon peak similar to that reported in previous studies [27–31] but not observed in experiments [1,26,34–38].

Thus, the additional terms $\varepsilon_{pl}$ from $\pi$ plasmon and $\varepsilon_\sigma$ from $\sigma$ electrons should be taking to into account when calculating the permittivity of the CNT walls. They lead to an increase in the depolarization field and introduce additional losses, which results in a decrease in frequency and height of the intersubband plasmon peak.

Previously, the discrepancy between theory and experiment in respect to frequency and height of intersubband plasmon peak are proposed to explain by the environmental effect due to the bundling of CNTs [1,28,33] and additional losses in the surrounding environment [32]. To elucidate the bundling effect from electromagnetic point of view, in the next section, we consider the transverse optical response from a bundle of doped CNTs.

## IV. INTERSUBBAND PLASMON IN DOPED CNT BUNDLE

In Appendix B, we develop the theory of electromagnetic wave scattering by a bundle of doped single-walled carbon nanotubes when the incident field is directed perpendicular to the CNT axis. We neglect the electron tunneling between the tubes in the bundle, and the electronic band structure in each CNT is supposed to be the same as in the individual CNT. Figure 5 shows the frequency dependencies of the normalized absorption cross section $\Lambda/S$ of a doped individual CNT, pair of CNTs, and bundle comprising seven CNTs in a the spectral range of the intersubband plasmon peak. The normalization is done to the surface area of all CNTs in the bundle [see (B17) in Appendix B]. As shown in Fig. 5, the plasmon resonance in a pair of CNTs shifts to lower frequencies for a field directed parallel to the long pair axis (dash-dot line), whereas a shifts to higher frequencies occurs for the orthogonal polarization (dashed line). Such behavior is typical for a dipole-dipole interaction and is observed for a pair of plasmon nanoparticles [49]. Let us also notice that the spectrum of $\Lambda/S$ for the bundle of seven CNTs is almost the same as for the individual CNT indicating that the bundling cannot influence significantly the frequency and height of the plasmon peak. We find that this is true for any almost circular bundles with $N \geqslant 7$. Thus, our calculations do not confirm a conclusion made in experimental paper [1] that an increase in the bundle size leads to a red shift of the plasmon frequency.

## V. CONCLUSIONS

We proposed a model of the effective optical permittivity of CNT film where the CNT wall permittivity was calculated from quantum theory of $\pi$-electron transitions and the contributions from $\pi$ plasmon and $\sigma$ electrons were taken into account phenomenologically. By choosing the $\pi$-plasmon parameters, we assumed that the real part of the averaged CNT wall permittivity in the spectral range 2–3 eV should be similar to that measured for graphene, other parameters were determined by fitting the experimental data for CNT film.

$\pi$-plasmon contribution to the CNT wall permittivity leads to an enhancement of the depolarization effect thus strongly suppressing the transverse response of undoped CNT in a spectral range below 4 eV. Also, this contribution together with one from the $\sigma$ electrons causes a red shift and reduction of intersubband plasmon peak in the absorbance spectrum of doped CNT thin film. Since the depolarization effect decreases with increasing the host permittivity, the azimuthal intersubband plasmon is observed in electrostatically doped CNTs in the liquid and in heavily doped CNTs in the air.

We developed the theory of optical scattering by a doped CNT bundle for the incident field polarized perpendicular to the bundle axis. We showed that the bundling cannot influence significantly the frequency and height of intersubband plasmon peak in the absorbance spectrum of doped CNT film.

## ACKNOWLEDGMENTS

V.A.S. was partly supported by HORIZON EUROPE Marie Sklodowska-Curie Actions (2021-PF-01, Project No. 101065500, TeraExc).

## APPENDIX A: THE SURFACE CONDUCTIVITY OF CNT

Here we shall represent the analytical formulas from Ref. [10] for calculating the surface conductivity $\sigma_{||}$ and $\sigma_\perp$ of a single-walled CNT along the axial and circumferential directions, respectively. We shall supplement those formulas with (A12), which takes into account intersubband transitions in doped CNTs. Also, we shall include phenomenologically the contribution from $\sigma$ electron to the CNT surface conductivity.

The permittivity of CNT in the framework of the linear response theory [10,12,13,27] is calculated as follows:

$$\varepsilon = 1 + \varepsilon_\sigma + \frac{8\pi e^2\hbar}{m_e^2\omega}\frac{1}{Sd}\sum_{\lambda,\lambda'=1,2}\sum_{N,N'}\int dk \times \int dk' \frac{|\langle N'k'\lambda'|\hat{p}|Nk\lambda\rangle|^2}{\epsilon_{\lambda'}(N',k') - \epsilon_\lambda(N,k) + \hbar\omega + i/\tau} \times \frac{f_{\lambda'}(N',k') - f_\lambda(N,k)}{\epsilon_{\lambda'}(N',k') - \epsilon_\lambda(N,k)}, \tag{A1}$$

where $\varepsilon_\sigma = 1.4$ takes phenomenologically into account the transitions from occupied $\sigma$ bands [19]; $e$ and $m_e$ are charge and mass of electron; $\hbar$ is the reduced Planck constant; $\hat{p}$ is the electron momentum; $k$ is a wave number; $\omega$ is angular frequency; $\tau$ is the time constant of the electron mean free path; the subscript $\lambda$ stands for the conduction ($\lambda = 2$) and valence ($\lambda = 1$) bands. $S$ and $d$ are the surface area and thickness of CNT wall, so that $Sd$ is a volume occupied by the CNT lattice. Since we use $\varepsilon_\sigma = 1.4$ the same as for graphite, the value of $d$ should be chosen equal to the interlayer distance in graphite, i.e., $d = 0.34$ nm. $\epsilon_\lambda(N,k)$ is an energy of 1D band with number $N$; $f_\lambda(N,k)$ is the Fermi function,

$$f_\lambda(N,k) = \left\{\exp\left[\frac{\epsilon_\lambda(N,k) - \mu}{k_B T}\right] + 1\right\}^{-1}, \tag{A2}$$

where $T$ is the absolute temperature; $k_B$ is the Boltzmann constant; $\mu$ is the chemical potential. $\mu = 0$ for undoped tubes, whereas $\mu = E_F$ for doped CNT, where $E_F$ is the Fermi energy.

Following Ref. [10], a tubule index $(a,b)$ satisfies $a \geqslant 1$ and $-a+1 \leqslant b \leqslant 0$. The axial surface conductivity of CNT is

$$\sigma_{||} = \frac{-i\omega d\left(\varepsilon_{||} - 1\right)}{4\pi}, \tag{A3}$$

where $d$ is the thickness of CNT wall and

$$\varepsilon_{||} = 1 + \varepsilon_\sigma + \varepsilon_{1||} + \varepsilon_{2||}. \tag{A4}$$

Here $\varepsilon_{1||}$ ($\varepsilon_{2||}$) is the contribution from the interband (intraband) transitions,

$$\varepsilon_{1||} = \left(\frac{e\hbar^2}{m_e}\right)^2 \frac{4\rho_C}{al_0}\sum_{N=0}^{a-1}\int_{-\pi/l_0}^{\pi/l_0} dk \frac{f_2(N,k) - f_1(N,k)}{\epsilon_2(N,k) - \epsilon_1(N,k)} \times \frac{(\mathrm{Re}\, K_0(N,k))^2}{\hbar^2\omega(\omega + i/\tau) - (\epsilon_2(N,k) - \epsilon_1(N,k))^2}, \tag{A5}$$

$$\varepsilon_{2||} = \left(\frac{e\hbar}{m_e}\right)^2 \frac{2\rho_C}{al_0}\frac{1}{\omega(\omega + i/\tau)}\sum_{N=0}^{a-1}\int_{-\pi/l_0}^{\pi/l_0} dk \times [\mathrm{Im}\, K_0(N,k)]^2\{f'[\epsilon_2(N,k)] + f'[\epsilon_1(N,k)]\}, \tag{A6}$$

where $l_0 = 1.5b_0$, $b_0 = 0.142$ nm is the in-plane C-C distance of the graphite; $\rho_C = \sqrt{3}/dl_0^2$ is the density of carbon atoms per volume in the graphene lattice;

$$\epsilon_{1,2}(N,k) = \mp\gamma_0\left\{1 + 4\cos\left(\frac{2\pi N}{a} - \frac{a+2b}{2a}kl_0\right)\times\cos\left(\frac{kl_0}{2}\right) + 4\cos\left(\frac{kl_0}{2}\right)^2\right\}^{1/2}. \tag{A7}$$

$\gamma_0 = 3.1$ eV is the hopping energy. $K_0(N,k)$ corresponds to the dimensionless matrix element of the momentum operator,

$$K_0(N,k) = \exp\left[-i\Theta(N,k)\right]\sum_{\lambda=1}^{3}\exp\left[-i\phi_\lambda(N,k)\right] \times [J_1\cos\eta_\lambda + J_2(1-\cos\eta_\lambda)^2]\xi_\lambda. \tag{A8}$$

$$\eta_1 = \frac{-\pi(a+b)}{a^2+ab+b^2}, \quad \xi_1 = \frac{-a+b}{3\sqrt{a^2+ab+b^2}},$$
$$\eta_2 = \frac{\pi b}{a^2+ab+b^2}, \quad \xi_2 = \frac{2a+b}{3\sqrt{a^2+ab+b^2}},$$
$$\eta_3 = \frac{\pi a}{a^2+ab+b^2}, \quad \xi_3 = \frac{-a-2b}{3\sqrt{a^2+ab+b^2}},$$

$$\phi_1(N,k) = 0, \quad \phi_2(N,k) = kl_0,$$
$$\phi_3(N,k) = \frac{2\pi N}{a} - \frac{b}{a}kl_0,$$

$$J_1 = \frac{-9e^{-u}}{20N_0}u^2\left(\frac{u^2}{3} + u + 1\right),$$

$$J_2 = \frac{-27R^2e^{-u}}{80l_0^2N_0}u^4(u+1), \quad u = \frac{Zl_0}{3a_{\mathrm{Bohr}}},$$

$$N_0 = 1 - \frac{9e^{-2u}}{4}\left(1 + u + \frac{2u^2}{5} + \frac{u^3}{15}\right)^2,$$

$$\Theta(N,k) = \arg\left\{\exp\left[-i\left(\frac{2\pi N}{a} - \frac{b}{a}kl_0\right)\right] + \exp[-ikl_0] + 1\right\},$$

where $R = \sqrt{3}b_0\sqrt{a^2+ab+b^2}/2\pi$ is a radius of CNT; $Z = 3.136$ is the "best atom" effective charge for carbon in units of electron charge $e$ for the $2p$ Slater orbital, $a_{\mathrm{Bohr}} = 5.29 \times 10^{-9}$. The notation $f'(\epsilon_{1,2}) = \partial f_{1,2}/\partial\epsilon_{1,2}$ is used in (A6).

The surface conductivity along circumferential direction of the CNT is

$$\sigma_\perp = \frac{-i\omega d(\varepsilon_\perp - 1)}{2\pi}, \tag{A9}$$

where

$$\varepsilon_\perp = 1 + \varepsilon_\sigma + \varepsilon_{1\perp} + \varepsilon_{2\perp}. \tag{A10}$$

The key point for further consideration is that $\varepsilon_\sigma$ is included into the CNT conductivity in Eq. (A9) thus influencing the

frequency of the azimuthal plasmon in CNTs via the denominator in (10). $\varepsilon_{\perp 1}$ ($\varepsilon_{\perp 2}$) is due to interband transitions between the conduction and valence bands (between subbands of the same band),

$$\varepsilon_{1\perp} = \chi\rho_C \sum_{N=0}^{a-1} \int_{-\pi/l_0}^{\pi/l_0} \frac{f_2(N+1,k+\kappa_0) - f_1(N,k)}{\epsilon_2(N+1,k+\kappa_0) - \epsilon_1(N,k)} \frac{\left|K_+(N+1,k+\kappa_0) + K_-^*(N,k)\right|^2}{\hbar^2\omega(\omega+i/\tau) - [\epsilon_2(N+1,k+\kappa_0) - \epsilon_1(N,k)]^2} dk, \tag{A11}$$

$$\varepsilon_{2\perp} = \frac{\chi\rho_C}{2} \sum_{N=0}^{a-1} \int_{-\pi/l_0}^{\pi/l_0} \frac{f_s(N+1,k+\kappa_0) - f_s(N,k)}{\epsilon_s(N+1,k+\kappa_0) - \epsilon_s(N,k)} \frac{\left|K_+(N+1,k+\kappa_0) - K_-^*(N,k)\right|^2}{\hbar^2\omega(\omega+i/\tau) - [\epsilon_s(N+1,k+\kappa_0) - \epsilon_s(N,k)]^2} dk. \tag{A12}$$

Here $s = 1$ ($s = 2$) for $p$-type ($n$-type) doping, and the asterisk means complex conjugation.

$$\kappa_0 = \frac{\pi(a+2b)}{l_0(a^2+ab+b^2)}, \quad \chi = \left(\frac{e\hbar^2}{\pi m_e}\right)^2 \frac{a^2+ab+b^2}{3al_0},$$

$$K_\pm(N,k) = \frac{1}{\sqrt{2}} \exp[-i\Theta(N,k)] \sum_{\lambda=1}^{3} \exp[-i\phi_\lambda(N,k)] \times [J_1(2\cos\eta_\lambda - 1) + J_2(1-\cos\eta_\lambda)^2] \times (1 - \exp(\pm i\eta_1)).$$

## APPENDIX B: THE TRANSVERSE RESPONSE OF CNT BUNDLE

Let a bundle of $\tilde{N}$ parallel doped CNTs be located in a host medium with permittivity $\kappa$ and exposed to the electromagnetic wave with an electric field perpendicular to the tube axis. We choose indexes $n$ and $m$ to enumerate CNTs in the bundle: $n, m = 1, 2 \ldots \tilde{N}$. Let $z$ axis of the cylindrical coordinate system $(\rho_n, \theta, z_n)$ coincides with the axis of the $n$th CNT, and the direction $\theta = 0$ coincides with the $x$ axis of the chosen Cartesian coordinate system (see Fig. 6). The incident field $E_0$ directed at an angle $\theta_0$ is assumed to be homogeneous within a bundle cross section.

We shall consider a frequency range nearby the intersubband transitions $(N,k) \to (N+1, k+\kappa_0)$ of doped CNT [see (A12)]. In this spectral range, predominantly two azimuthal modes of the surface current density are excited along the circumferential direction in the $n$th CNT [27],

$$j_n(\theta) = \sum_l j_n^{(l)} \exp(il\theta), \tag{B1}$$

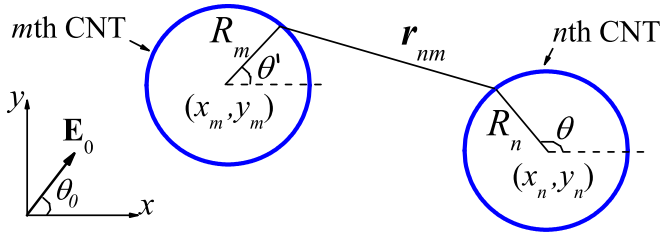


FIG. 6. Geometry of $m$th and $n$th CNTs.

where $l = -1, +1$. Ohm's law is valid for each mode

$$j_n^{(l)} = \sigma_n^{(l)} \left( E_{0n}^{(l)} + \sum_{m=1}^{\tilde{N}} E_{nm}^{(l)} \right), \tag{B2}$$

where $\sigma_n^{(l)}$ is the surface conductivity of the $n$th CNT for the $l$th mode. Note that $\sigma_n^{(+1)} = \sigma_n^{(-1)} = \sigma_n$ is true in the absence of the Aharonov-Bohm flux along the tube axis [27]; $\sigma_n = \sigma_\perp + \sigma_{pl}$ [see (A9) and (3) for $\sigma_\perp$ and $\sigma_{pl}$]. $E_{0n}^{(l)}$ is an azimuthal component of the incident field responsible for the $l$th mode excitation,

$$E_{0n}^{(l)} = \frac{-1}{2\pi} \int_0^{2\pi} E_0 \sin(\theta - \theta_0) \exp(-il\theta) d\theta. \tag{B3}$$

$E_{nm}^{(l)}$ is an azimuthal component of the field scattered by the $m$th CNT on a surface of the $n$th CNT,

$$E_{nm}^{(l)} = \frac{1}{2\pi} \int_0^{2\pi} E_{nm}(\theta) \exp(-il\theta) d\theta, \tag{B4}$$

$$E_{nm}(\theta) = -\frac{1}{R_n} \frac{\partial\varphi_{nm}}{\partial\theta}. \tag{B5}$$

Here $R_n$ is a radius of $n$th CNT; $\varphi_{nm}$ is the electric potential created on a surface of the $n$th CNT by the surface charge density $\rho_m^{(l)}$ of the $m$th CNT [25],

$$\varphi_{nm}(\theta) = \frac{-2R_m}{\kappa} \int_0^{2\pi} \sum_l \rho_m^{(l)} e^{il\theta'} \ln[r_{nm}(\theta,\theta')] d\theta', \tag{B6}$$

where

$$r_{nm}(\theta,\ \theta') = \{(x_m + R_m\cos\theta' - x_n - R_n\cos\theta)^2 + (y_m + R_m\sin\ \theta' - y_n - R_n\sin\theta)^2\}^{1/2} \tag{B7}$$

is a distance between two points on the $m$th and $n$th CNTs (see Fig. 6). The meaning of $x_{m,n}$, $y_{m,n}$, $\theta$ and $\theta'$ is clear from Fig. 6, where the $m$th and $n$th CNTs are shown. Equation (B6) gives the potential of the field scattered by the $m$th CNT in the point with coordinates $(\rho, \theta)$, if one supposes $x_n = x_m$, $y_n = y_m$, and $R_n = \rho$ in (B7).

The continuity equation

$$\frac{\partial}{\partial t}\rho_m^{(l)} \exp(il\theta - i\omega t) + \frac{1}{R_m}\frac{\partial}{\partial\theta} j_m^{(l)} \exp(il\theta - i\omega t) = 0 \tag{B8}$$

yields the relation between the surface current and charge densities

$$\rho_m^{(l)} = \frac{l}{\omega R_m} j_m^{(l)}. \tag{B9}$$

Subsequent substitution of (B9), (B6), and (B5) in (B4) with the following integration at $m = n$ yields

$$E_{nm}^{(l)} = \sum_{l'=+1,-1} M_{nm}^{(ll')} j_m^{(l')}, \tag{B10}$$

$$M_{nn}^{(ll')} = -\frac{i2\pi}{\kappa R_n \omega}, \tag{B11}$$

$$M_{nm,\ n\neq m}^{(ll')} = \frac{l'}{\pi\omega\kappa R_n}\int_0^{2\pi} d\theta \times \frac{\partial}{\partial\theta}\left[\int_0^{2\pi} \exp(il'\theta')\ln[r_{nm}(\theta,\theta')]d\theta'\right] \times \exp(-il\theta). \tag{B12}$$

Substituting (B10) in (B2) and taking into account (B12), we arrive at a system of $2\tilde{N}$ equations for the surface current density

$$j_n^{(l)}\left[\frac{1}{\sigma_n^{(l)}} + \frac{i2\pi}{\kappa R_n \omega}\right] - \sum_{m=1,\neq n}^{\tilde{N}} \sum_{l'=+1,-1} M_{nm}^{(ll')} j_m^{(l')} = E_{0n}^{(l)}. \tag{B13}$$

The solution of Eq. (B13) allows us to obtain the transverse polarizability of CNT bundle per unit length

$$\alpha_b = \sum_{n=1}^{\tilde{N}} \frac{-iR_n}{\omega E_0}\int_0^{2\pi} j_n(\theta)\sin(\theta-\theta_0)d\theta, \tag{B14}$$

where sin(.) appears due to the current projection on the direction of the incident field. Substitution of (B1) into (B14) followed by integration yields

$$\alpha_b = \sum_{n=1}^{\tilde{N}} \frac{\pi R_n}{\omega E_0}\sum_l l\exp(il\theta_0) j_n^{(l)}. \tag{B15}$$

The transverse polarizability of the individual $n$th CNT per unit length can be found as

$$\alpha_n = \frac{i\pi\sigma_n R_n}{\omega}\left(1 + \frac{i2\pi\sigma_n}{\omega R_n \kappa}\right)^{-1}. \tag{B16}$$

The absorption cross section $\Lambda$ of the bundle normalized to the surface area $S$ of all the tubes is

$$\Lambda/S = \frac{2\omega}{c\sum_{n=1}^{\tilde{N}} R_n}\mathrm{Im}\ \alpha_b, \tag{B17}$$

where $c$ is the speed of light in vacuum.


[1] D. Satco, D. S. Kopylova, F. S. Fedorov, T. Kallio, R. Saito, and A. G. Nasibulin, ACS Appl. Electron. Mater. **2**, 195 (2020).
[2] G. Fanchini, S. Miller, B. B. Parekh, and M. Chhowalla, Nano Lett. **8**, 2176 (2008).
[3] G. A. Ermolaev, A. P. Tsapenko, V. S. Volkov, A. S. Anisimov, Y. G. Gladush, and A. G. Nasibulin, Appl. Phys. Lett. **116**, 231103 (2020).
[4] T. M. Barnes, J. van de Lagemaat, D. Levi, G. Rumbles, T. J. Coutts, C. L. Weeks, D. A. Britz, I. Levitsky, J. Peltola, and P. Glatkowski, Phys. Rev. B **75**, 235410 (2007).
[5] Y. Battie, D. Jamon, A. En Naciri, J.-S. Lauret, and A. Loiseau, Appl. Phys. Lett. **102**, 091909 (2013).
[6] Y. Battie, D. Jamon, J.-S. Lauret, A. E. Naciri, L. Broch, and A. Loiseau, Carbon **50**, 4673 (2012).
[7] Y. Battie, M. Dossot, N. Allali, V. Mamane, A. E. Naciri, L. Broch, and A. V. Soldatov, Carbon **96**, 557 (2016).
[8] S. Schöche, P.-H. Ho, J. A. Roberts, S. J. Yu, J. A. Fan, and A. L. Falk, J. Vac. Sci. Technol. B **38**, 014015 (2020).
[9] Y. Battie, L. Broch, A. E. Naciri, J.-S. Lauret, M. Guézo, and A. Loiseau, Carbon **83**, 32 (2015).
[10] S. Tasaki, K. Maekawa, and T. Yamabe, Phys. Rev. B **57**, 9301 (1998).
[11] E. Malić, M. Hirtschulz, F. Milde, A. Knorr, and S. Reich, Phys. Rev. B **74**, 195431 (2006).
[12] M. S. Dresselhaus, G. Dresselhaus, and P. Avouris, *Carbon Nanotubes* (Springer, Berlin, 2001).
[13] M. F. Lin and K. W.-K. Shung, Phys. Rev. B **50**, 17744 (1994).
[14] Y. Takagi and S. Okada, Phys. Rev. B **79**, 233406 (2009).
[15] S. Ohmori, T. Saito, M. Tange, B. Shukla, T. Okazaki, M. Yumura, and S. Iijima, J. Phys. Chem. C **114**, 10077 (2010).
[16] M. S. Ukhtary and R. Saito, Carbon **167**, 455 (2020).
[17] M. A. El-Sayed, G. A. Ermolaev, K. V. Voronin, R. I. Romanov, G. I. Tselikov, D. I. Yakubovsky, N. V. Doroshina, A. B. Nemtsov, V. R. Solovey, A. A. Voronov *et al.*, Nanomaterials **11**, 1230 (2021).
[18] K. F. Mak, J. Shan, and T. F. Heinz, Phys. Rev. Lett. **106**, 046401 (2011).
[19] E. Taft and H. Philipp, Phys. Rev. **138**, A197 (1965).
[20] L. Yang, J. Deslippe, C.-H. Park, M. L. Cohen, and S. G. Louie, Phys. Rev. Lett. **103**, 186802 (2009).
[21] J. Scott, Rev. Mod. Phys. **46**, 83 (1974).
[22] H.-L. Liu, B. D. Annawati, N. T. Hung, D. P. Gulo, P. Solís-Fernández, K. Kawahara, H. Ago, and R. Saito, Phys. Rev. B **107**, 165421 (2023).
[23] R. B. Payod, D. Grassano, G. N. C. Santos, D. I. Levshov, O. Pulci, and V. A. Saroka, Nat. Commun. **11**, 82 (2020).
[24] H. Ajiki and T. Ando, Phys. B: Condens. Matter **201**, 349 (1994).
[25] T. Ando, J. Phys. Soc. Jpn. **74**, 777 (2005).
[26] T. Igarashi, H. Kawai, K. Yanagi, N. T. Cuong, S. Okada, and T. Pichler, Phys. Rev. Lett. **114**, 176807 (2015).
[27] K. I. Sasaki and Y. Tokura, Phys. Rev. Appl. **9**, 034018 (2018).
[28] D. Satco, A. R. T. Nugraha, M. S. Ukhtary, D. Kopylova, A. G. Nasibulin, and R. Saito, Phys. Rev. B **99**, 075403 (2019).
[29] R. Saito, M. S. Ukhtary, S. Wang, and Y. Iwasaki, J. Appl. Phys. **128**, 164301 (2020).
[30] F. J. García de Abajo, ACS Photonics **1**, 135 (2014).
[31] K. I. Sasaki, S. Murakami, and H. Yamamoto, Appl. Phys. Lett. **108**, 163109 (2016).
[32] K. I. Sasaki, Carbon **160**, 1 (2020).
[33] J. Jiang, R. Saito, G. G. Samsonidze, A. Jorio, S. G. Chou, G. Dresselhaus, and M. S. Dresselhaus, Phys. Rev. B **75**, 035407 (2007).

[34] D. S. Kopylova, D. A. Satco, E. M. Khabushev, A. V. Bubis, D. V. Krasnikov, T. Kallio, and A. G. Nasibulin, Carbon **167**, 244 (2020).
[35] F. Wang, D. Yang, L. Li, Y. Liu, X. Wei, W. Zhou, H. Kataura, H. Liu, and S. Xie, Adv. Funct. Mater. **32**, 2107489 (2022).
[36] K. Yanagi, R. Okada, Y. Ichinose, Y. Yomogida, F. Katsutani, W. Gao, and J. Kono, Nat. Commun. **9**, 1121 (2018).
[37] S. Kazaoui, N. Minami, N. Matsuda, H. Kataura, and Y. Achiba, Appl. Phys. Lett. **78**, 3433 (2001).
[38] K. Yanagi, R. Moriya, Y. Yomogida, T. Takenobu, Y. Naitoh, T. Ishida, H. Kataura, K. Matsuda, and Y. Maniwa, Adv. Mater. **23**, 2811 (2011).
[39] O. T. Zaremba, A. E. Goldt, E. M. Khabushev, A. S. Anisimov, and A. G. Nasibulin, Mater. Sci. Eng. B **278**, 115648 (2022).
[40] A. E. Goldt, O. T. Zaremba, M. O. Bulavskiy, F. S. Fedorov, K. V. Larionov, A. P. Tsapenko, Z. I. Popov, P. Sorokin, A. S. Anisimov, H. Inani *et al.*, J. Mater. Chem. C **9**, 4514 (2021).
[41] A. P. Tsapenko, S. A. Romanov, D. A. Satco, D. V. Krasnikov, P. M. Rajanna, M. Danilson, O. Volobujeva, A. S. Anisimov, A. E. Goldt, and A. G. Nasibulin, J. Phys. Chem. Lett. **10**, 3961 (2019).
[42] A. V. Melnikov, P. P. Kuzhir, S. A. Maksimenko, G. Y. Slepyan, A. Boag, O. Pulci, I. A. Shelykh, and M. V. Shuba, Phys. Rev. B **103**, 075438 (2021).
[43] M. Y. Sfeir, F. Wang, L. Huang, C.-C. Chuang, J. Hone, S. P. O'Brien, T. F. Heinz, and L. E. Brus, Science **306**, 1540 (2004).
[44] V. Gubarev, M. Krivokorytov, V. Krivtsun, N. Novikova, S. Yakunin, A. Pal, J. A. Ramirez B, D. Krasnikov, V. Medvedev, and A. Nasibulin, J. Appl. Phys. **133**, 095106 (2023).
[45] G. Ya. Slepyan, S. A. Maksimenko, A. Lakhtakia, O. Yevtushenko, and A. V. Gusakov, Phys. Rev. B **60**, 17136 (1999).
[46] M. V. Shuba, A. G. Paddubskaya, A. O. Plyushch, P. P. Kuzhir, G. Ya. Slepyan, S. A. Maksimenko, V. K. Ksenevich, P. Buka, D. Seliuta, I. Kasalynas, J. Macutkevic, G. Valusis, C. Thomsen, and A. Lakhtakia, Phys. Rev. B **85**, 165435 (2012).
[47] I. V. Bondarev and C. M. Adhikari, Phys. Rev. Appl. **15**, 034001 (2021).
[48] P. Petit, C. Mathis, C. Journet, and P. Bernier, Chem. Phys. Lett. **305**, 370 (1999).
[49] W. Rechberger, A. Hohenau, A. Leitner, J. Krenn, B. Lamprecht, and F. Aussenegg, Opt. Commun. **220**, 137 (2003).